arXiv:1609.09144v1 [physics.bio-ph] 28 Sep 2016

Mapping orientational and microstructural metrics of neuronal integrity with *in vivo* diffusion MRI

Dmitry S. Novikov,* Jelle Veraart, Ileana O. Jelescu, and Els Fieremans
Bernard and Irene Schwartz Center for Biomedical Imaging, Department of Radiology, New York University School of Medicine, New York, NY 10016, USA

(Dated: September 23, 2016)

Diagnosis of brain disorders is hindered by the lack of an imaging technique that reveals the architecture of neuronal tissue at the cellular level, where the associated pathological processes develop. Accessing tissue integrity at the micrometer scale, three orders of magnitude below MRI resolution, would be akin to super-resolution in microscopy. For MRI, bridging the resolution gap relies on biophysical modeling of water diffusion hindered by cell walls. Here we develop a general framework for estimating orientational and microstructural parameters of neurites (axons and dendrites). By employing a set of rotational invariants, we analytically reveal the nontrivial topology of parameter estimation landscape, showing that multiple branches of parameters describe the measurement almost equally well, with only one of them corresponding to the biophysical reality. A comprehensive acquisition shows that the branch choice differs for white and for gray matter. Our framework reveals hidden degeneracies in MRI parameter estimation for neuronal tissue, provides microstructural and orientational maps in the whole brain without constraints or priors, and connects modern biophysical modeling with clinical MRI.

Brownian motion of water molecules is strongly hindered by neurite walls[1]. Serendipitously, this sensitivity to tissue microstructure can be probed with NMR for diffusion times $t \sim 1 - 1000\,\text{ms}$, corresponding to a diffusion length (rms molecular displacement) $\ell(t) \sim 1 - 50\,\mu\text{m}$ commensurate with cell dimensions. The resulting diffusion MRI (dMRI) signal, acquired over a macroscopic imaging voxel, is an indirect but powerful probe into tissue microstructure at the scale $\ell(t)$, 2-3 orders of magnitude below the imaging resolution.

The dMRI signal is generally anisotropic[1,2], non-Gaussian[1–12], and time-dependent[13–15]. Description of this complex process simplifies at long diffusion times $t \sim 100\,\text{ms}$, used in clinical dMRI, when $\ell(t) \sim 10\,\mu\text{m}$ exceeds typical neurite diameters $a \lesssim 1\,\mu\text{m}$. In this regime, diffusion approaches its Gaussian limit separately in the intra- and extra-neurite spaces, Fig. 1. Biologically distinct hindrances lead to coarse-grained diffusion coefficients inside (D_a) and outside ($D_e^\parallel$ and $D_e^\perp$) neurites within an elementary fiber fascicle; transverse diffusion $\sim a^2/t \ll D_a$ inside neurites becomes negligible. The dMRI signal (voxel-averaged diffusion propagator) is an ensemble average over contributions of individual fascicles within a voxel.

Here we investigate in detail the general picture of anisotropic Gaussian compartments, Fig. 1, as an overarching model, such that previously used models[3–12] follow as special cases. The dMRI signal parameterized by diffusion weighting $b = q^2 t$

$$S_{\hat{\mathbf{g}}}(b) = S(0) \cdot \int_{|\hat{\mathbf{n}}|=1} \mathrm{d}\hat{\mathbf{n}}\, \mathcal{P}(\hat{\mathbf{n}})\, \mathcal{K}(b, \hat{\mathbf{g}}\cdot\hat{\mathbf{n}}) \qquad (1)$$

and measured in the unit direction $\hat{\mathbf{g}}$, is a convolution (on a unit sphere) between the fiber orientation distribution function (ODF) $\mathcal{P}(\hat{\mathbf{n}})$, and the response

$$\mathcal{K}(b,\xi) = f e^{-bD_a\xi^2} + (1-f) e^{-bD_e^\perp - b(D_e^\parallel - D_e^\perp)\xi^2} \qquad (2)$$

from a perfectly aligned fiber segment (fascicle) pointing in the direction $\hat{\mathbf{n}}$. The kernel (2) depends on the relative angle θ, $\cos\theta \equiv \xi = \hat{\mathbf{g}}\cdot\hat{\mathbf{n}}$. It is a sum of the exponential (in b) contributions from intra- and extra-neurite spaces, with T_2-weighted water fractions f and $1-f$. Compartments such as isotropic cerebrospinal fluid (CSF), can in principle be added to kernel (2); here we will study in depth the two-compartment kernel (2), and will later comment on its generalizations.

The scalar parameters f, D_a, $D_e^\parallel$ and $D_e^\perp$, and ODF $\mathcal{P}(\hat{\mathbf{n}})$, carry distinct biophysical significance. Deconvolving voxel-wise fiber ODF, instead of relying on the empirical directions from the signal (1), provides a much more adequate starting point for fiber tractography, an essential tool for mapping structural brain connectivity and for presurgical planning.

The scalar parameters of the kernel (2) make dMRI measurements specific to μm-level manifestations of disease processes, such as demyelination[16,17] ($D_e^\perp$), axonal loss[17] (f), beading[18], oedema and inflammation (D_a and $D_e^\parallel$). Since the precise nature and pathological changes in microarchitecture of restrictions leading to D_a, $D_e^\parallel$ and $D_e^\perp$ values are unknown, ideally, to become specific to pathology, one needs to estimate f, D_a, $D_e^\parallel$ and $D_e^\perp$ sepearately, without constraints or priors.

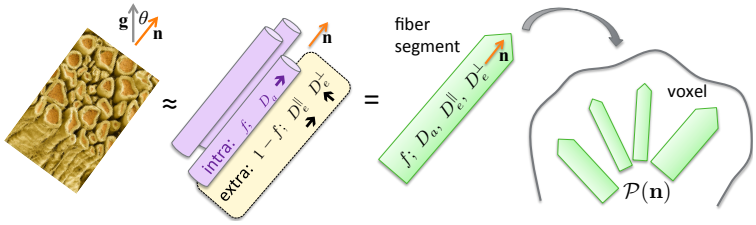


FIG. 1. **Overarching model of diffusion in neuronal tissue.** In the long time limit, elementary fiber segments (fascicles), consisting of intra- and extra-neurite compartments, are described by at least 4 independent parameters: f, D_a, $D_e^\parallel$ and $D_e^\perp$. Within a macroscopic imaging voxel, such segments contribute to the directional dMRI signal according to their ODF $\mathcal{P}(\hat{\mathbf{n}})$. Due to its rich orientational content, the total number of parameters characterizing a voxel ranges between 30 – 50, making direct nonlinear fitting of equations (1) and (2) to noisy data suffer from poor accuracy and precision.

To quantify the problem's complexity, let us find how many parameters N_p should the model (1) have. The answer depends on the maximal power $l_{\max}$ of the diffusion weighting $b^{l_{\max}/2} \sim q^{l_{\max}}$ to which an acquisition is sensitive, at a given signal-to-noise ratio (SNR). This can be seen from Taylor expansion of signal (1) (normalized to $S(0) \equiv 1$ from now on)

$$S_{\hat{\mathbf{g}}}(b) = 1 - bM^{(2)}_{i_1 i_2}\, g_{i_1} g_{i_2} + \frac{b^2}{2!}\, M^{(4)}_{i_1 \dots i_4}\, g_{i_1} \dots g_{i_4} - \dots \quad (3)$$

in the fully symmetric moments $M^{(l)}_{i_1 \dots i_l}$, where Einstein's convention of summation over pairs of repeating indices is assumed. The highest-order moment $M^{(l_{\max})}$ still resolvable from the signal sets the maximal order $l_{\max}$ for the even-order spherical harmonics (SH) expansion of the ODF $\mathcal{P}(\hat{\mathbf{n}}) = 1 + \sum_{l=2,4,\dots}^{l_{\max}} \sum_{m=-l}^{l} p_{lm} Y_{lm}(\hat{\mathbf{n}})$. Hence, the (minimum) 4 *scalar* parameters from the kernel (2) are complemented by the $n_c(l_{\max}) - 1$ *tensor* parameters p_{lm}, where $n_c(l) = \sum_{l'=0,2,\dots}^{l} (2l'+1) = \frac{1}{2}(l+1)(l+2)$ is the number of independent components of $M^{(l)}$, yielding $N_p(l_{\max}) = 4 + l_{\max}(l_{\max}+3)/2 = 9,\ 18,\ 31,\ 48,\ \dots$ for $l_{\max} = 2,\ 4,\ 6,\ 8,\ \dots$.

This parameter counting reveals that the model complexity grows fast, as $l^2_{\max}$, accounting for the rich orientational content of the realistic fiber ODFs in the brain. For practical $l_{\max} \sim 4 - 8$, the dMRI signal in principle "contains" a few dozen parameters, none of which are known *a priori*. Because of such high dimensionality of parameter space, direct nonlinear fitting of equations (1) and (2) to realistic noisy data has been extremely unreliable. Hence, parameter estimation from clinical acquisitions has so far reverted to making severe restrictions on the ODF shape: either assuming a highly aligned bundle[8,9], or a special Gaussian-like ODF shape characterized by one[10] or two[19] parameters, in order to reduce the dimensionality of the problem, from $\sim 30 - 50$ down to ~ 3.

However, even assuming a 1-parameter ODF shape[10], unconstrained nonlinear fitting has recently revealed multiple biophysically plausible minima in the (4+1)-dimensional parameter space, and shallow directions along them[20]. Current clinical data has been mostly analyzed by fixing[10,19] all diffusion coefficients in equation (2) and ODF shape $\mathcal{P}(\hat{\mathbf{n}})$ in equation (1), introducing *a priori* unknown bias[20] for the remaining few parameters, and thereby losing specificity — the main advantage of employing microstructural modeling.

Results

Here we show that it is possible to estimate all the parameters of problem (1) and (2) without making any assumptions about the ODF shape and about the scalar parameter values of the kernel (2) and their priors, in about 10 minutes on a desktop computer for the whole brain dMRI data set. For that, we will first factorize equation (1) in the SH basis, in order to separate the estimation of scalar parameters $x \equiv \{f, D_a, D_e^{\parallel}, D_e^{\perp}\}$ from tensor ODF SH coefficients p_{lm}. We will see that the ODF-independent estimation of the scalar parameters in the space of rotational invariants is generally *degenerate*, and we will analytically uncover the nontrivial topology of the minimization landscape, Fig. 2.

Out of the two "branches" $x_{\pm}$ of parameters, corresponding to the two trenches in the landscape, only one will correspond to the biophysical reality, and the other one should be discarded. Branch selection, Fig. 3, will turn out to be nontrivial, and generally brain region-specific. Based on the branch choice, we will produce parameter maps and the fiber ODFs in the whole brain, Fig. 4, and critically assess the previously used constraints, Fig. 5.

Factorization and Rotational Invariants. The problem (1)–(2) factorizes in the SH basis[5],

$$S_{lm}(b, x) = p_{lm}\, K_l(b, x)\,. \quad (4)$$

Here S_{lm} are SH coefficients of the signal (1), and $K_l(b, x)$ are projections of the kernel (2) onto the Legendre polynomials (equation (9) in the *Methods* section) for a given set $x = \{f, D_a, D_e^{\parallel}, D_e^{\perp}\}$ of scalar parameters. To factor out the dependence on the choice of the basis (via $m = -l \dots l$), recall that any rotation corresponds to an orthogonal transformation on the $(2l+1)$-dimensional vectors S_{lm} and p_{lm}, belonging to the irreducible representation of the SO(3) group labeled by "angular momentum" index l. Hence, the 2-norms $\|S_l\|^2 = \sum_{m=-l}^{l} |S_{lm}|^2$ and $\|p_l\|^2 = \sum_{m=-l}^{l} |p_{lm}|^2$ are invariant. Introducing basis-independent *rotational invariants* $S_l \equiv \|S_l\|/\mathcal{N}_l$ and $p_l \equiv \|p_l\|/\mathcal{N}_l$ of the signal and ODF, where normalization $\mathcal{N}_l = \sqrt{4\pi(2l+1)}$ is chosen so that $0 \le p_l \le 1$, we can factor out ODF parameters p_{lm}:

$$S_l(b, x) = p_l\, K_l(b, x)\,, \quad l = 0,\ 2,\ \dots\,. \quad (5)$$

Here, $p_0 \equiv 1$ (ODF normalization); the remaining ODF invariants p_l, one for each l, characterize its anisotropy, as it will be discussed below.

It now appears logical to first estimate the scalar parameters x, together with just a few basis-independent p_l, $l = 0, 2, \dots$, from the greatly reduced system of equations (5), one for each l. A standard way to solve such system is to minimize the corresponding rotationally invariant (RotInv) "energy" function

$$F^2(x, \{p_l\}) \equiv \frac{1}{\left(1 + \frac{L}{2}\right) N_b} \sum_{l=0,2,\dots}^{L} \sum_{j=1}^{N_b} [S_l(b_j, x) - p_l K_l(b_j, x)]^2 \quad (6)$$

with respect to x and a few p_l, $l = 0, 2, \dots, L$. Here b_j are the radii of N_b shells in q-space for a usual spherical sampling; all units for diffusion coefficients and for $1/b$ are $\mu\mathrm{m}^2/\mathrm{ms}$.

The estimated scalar parameters x will allow us to reconstruct the kernel components $K_l(b, x)$, and to subsequently evaluate all ODF coefficients p_{lm} using equation (4), based on the linearly estimated S_{lm} from the measured signal.

Topology of Parameter Landscape. While the above rotationally invariant framework looks conceptually simple and completely general, the rest of this paper will be devoted to uncovering and resolving hidden degeneracies of parameter estimation problem (1) because of the kernel (2) specific to multi-compartmental diffusion in neuronal tissue.

The contour plots of F-values, equation (6), shown in Fig. 2 (cf. also Supplementary Figs. S1–S2 for more examples), illustrate that the minimization landscape is generally quite *flat*

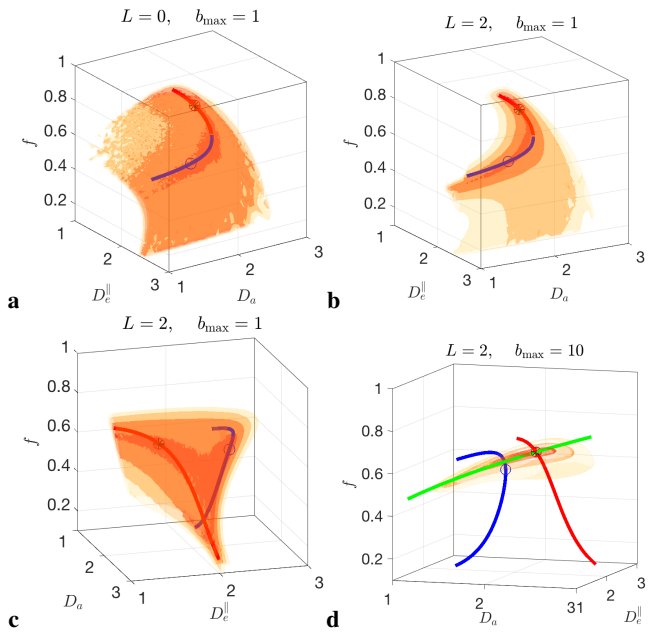


FIG. 2. **Degeneracies in scalar parameter estimation** depending on the maximal invariant L used, equation (6). Low-"energy" landscape of RotInv problem (6) for system (5) is a 2-dimensional surface for $l = 0$ invariant (**a**), and two 1-dimensional trenches with $l = 0,\ 2$ invariants included (**b, c**). The trenches can either match to form a single 1-dimensional manifold (**b**), or be disjoint (**c, d**), depending on the ground truth values (see Supplementary Figs. S1–S2). Circles denote minima in both trenches, with the true minimum marked by $*$. Exact branches $\zeta = \pm$ of system (18) (cf. *Methods*) are drawn in red and blue, reproducing the trenches up to $\mathcal{O}(b^2)$. Including large b data further limits the landscape to the surface $f/\sqrt{D_a} = \text{const}$ arising solely from intra-neurite space[21] (green section in **d**).

in at least 1 dimension, and there are distinct *multiple minima*. We emphasize from the outset that these degeneracies are *intrinsic* to the problem (1), and are not introduced by the above RotInv framework or the particular way (6) of solving the system (5). Rather, this framework allows us to uncover their general origin – namely, the multi-compartmental character of the kernel (2).

We now focus on the topology of the low-energy landscape of F in order to understand degeneracies in parameter estimation, which is crucial for initializing the search for parameters x within the biophysically correct domain, and for speeding up the solution of system (5). Our analytical method will be approximating the signal (1) by its low-b expansion (3), whose consecutive terms are equivalent to diffusion tensor imaging (DTI, $\sim b$), diffusion kurtosis imaging (DKI, $\sim b^2$), etc. Empirically, it is well known that DKI[22] approximates clinical dMRI signal ($b_{\max} \sim 1 - 2$) quite well, further justifying studying the series (3) up to $\mathcal{O}(b^2)$, and perhaps, up to $\mathcal{O}(b^3)$.

For low enough b (typically used in clinic), nonlinear fitting (6) practically corresponds to matching first few moments of the signal (3) to those of the model (1). In *Methods* we exactly derive this matching, the LEMONADE system (18), for up to $\mathcal{O}(b^3)$. We can now calculate the dimensionality of the low-energy manifolds in Fig. 2 by a simple counting of constraints.

Taking the $l = 0$ invariant alone, $S_0 = K_0$, is equivalent to isotropic signal averaging[23–26]. Expanding this relation up to $\mathcal{O}(b^2)$ yields a 2-dimensional *surface*, in accord with the two constraints (18a) ($\sim b$) and (18c) ($\sim b^2$) for the 4 scalar parameters x, cf. Fig. 2a (note that isotropic averaging discards nontrivial p_l with $l > 0$). We can see that determining all 4 scalar parameters from the $L = 0$ invariant requires the sensitivity to the signal's moments $M^{(8)}$ (their full traces), up to b^4, which is practically very difficult to achieve. Intuitively, it is quite obvious that discarding the orientational content makes parameter estimation less informative.

Staying at the same level $\mathcal{O}(b^2)$, and including the $K_2(b)$ invariant, $L = 2$, adds one extra parameter p_2 describing the sensitivity to the lowest-order ODF anisotropy, and two extra equations, turning the surface into the two narrow 1-dimensional *trenches* in parameter space, Fig. 2b,c (the first 4 equations of the system (18) for x and p_2). Having a shallow trench is obvious from the counting of constraints; getting *two* trenches is nontrivial.

The two trenches $f_\zeta(p_2)$ (equation (26) in *Methods*), labeled by branch index $\zeta = \pm$, are exactly derived as the two branches of quadratic equation (22) that involves rotationally invariant combinations of signal's moment tensors $M^{(2)}$ and $M^{(4)}$. Physically, the dual branches come from having two tissue compartments, cf. subsection *Multiple minima: A toy model* in *Methods*. There, we emphasize that both sets of values can look perfectly plausible, and the "wrong" set corresponds to swapping intra- and extra-neurite parameters — which carries the danger of completely misrepresenting parameter changes in pathology. Including the $K_4(b)$ invariant adds one extra parameter p_4 and only one equation (since $K_l(b)|_{b\to 0} \sim b^{l/2}$); hence, additional invariants $K_{l>2}$ do not provide extra constraints up to b^2.

As a result, if an acquisition is only sensitive to $\mathcal{O}(b^2)$, due to e.g. b-range or SNR limitations, the parameter estimation problem will be "doubly degenerate", as we empirically observed recently for a particular ODF shape[20]: with respect to selecting the trench, and due to the perfect flatness of either trench. Our exact solution of system (18) establishes that this degeneracy and flatness are general "hidden" features of problem (1)–(2), explained by every point in each branch exactly matching the b and b^2 terms in the Taylor expansion (3).

Furthermore, the above RotInv analysis reveals that simplistic counting of parameters, without separating them into the scalar and ODF parts, can be misleading. Indeed, while the lowest two moment tensors $M^{(2)}$ and $M^{(4)}$, corresponding to $l_{\max} = 4$, contain $N_c(4) = 21$ nonequivalent parameters (cf. equation (14) in *Methods*, akin to the number of DKI parameters), they are not enough to determine the corresponding $N_p(4) = 18$ model parameters (as calculated after equation (3)), since the excess parameters over-determine the ODF, whereas the kernel (2) remains under-determined. (This issue becomes even more severe if the kernel has more than 2 compartments.) This means that, unfortunately, popular DKI acquisition is not enough to resolve two-compartment model parameters due to a perfect 1-dimensional degeneracy within a chosen trench, unless, e.g., p_2 is fixed by the ODF shape: $p_2 \to 1$, the aligned fibers assumption[8,9].

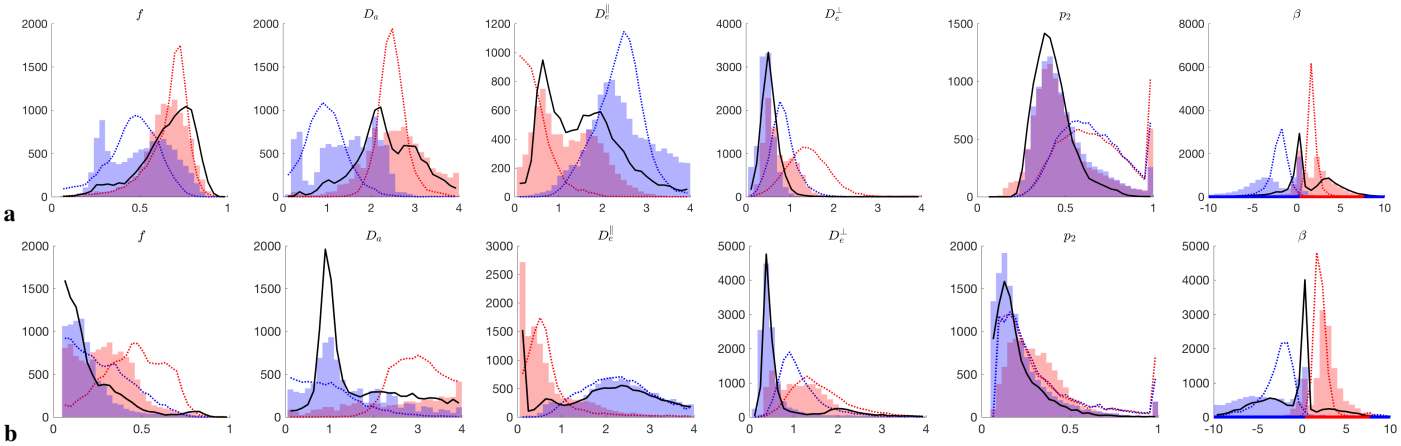


FIG. 3. **Degeneracy in parameter estimation with human dMRI data. Branch selection.** Parameter histograms for white matter, **a**, and for gray matter, **b**. Red/blue dashed histograms correspond to $\zeta = \pm$ solutions $\{f, D_a, D_e^{\parallel}, D_e^{\perp}, p_2\}_{\pm}$ of LEMONADE system (18); filled histograms are obtained via RotInv fitting (6) up to $b \leq 10$, initialized by the $\zeta = \pm$ solutions of system (18). Solid black histogram is the outcome of the prevalence method, which mostly agrees with $\zeta = +$ in WM and with $\zeta = -$ in GM, cf. histograms of the branch ratio β falling within red/blue intervals, equation (7), and Supplementary Fig. S3 for the branch index maps.

We also note that including the $l > 0$ invariants in system (5) is only possible for anisotropic ODFs, with $p_l > 0$. Physically, it is expected since the less symmetric the system, the more inequivalent ways it enables for probing it; this intuition underlies theory of excitations of non-spherical nuclei[27]. In the brain, the ODF is at least somewhat anisotropic; the simplest parameter p_2, dominated by $p_{20} \equiv (3\langle\cos^2\theta\rangle - 1)/2$, is generally nonzero even in the gray matter, as we can see *a posteriori*, cf. Figs. 3 and 4.

Bimodality of parameter estimation in human dMRI. In Fig. 3 we demonstrate the double degeneracy of parameter estimation problem (1) and (2), anticipated from Fig. 2, using a dedicated human dMRI acquisition. We used a broad range of $b = 0\ldots10\,\mathrm{ms}/\mu\mathrm{m}^2$ distributed over 21 shells, 64 directions each shell, on 3 healthy volunteers (data for subject #1 is shown). After denoising, Gibbs and Rician bias correction, and moment estimation via cumulant expansion (see *Methods*), we first solve the LEMONADE system (18) (using subset with $b \leq 2.5$, a proxy for clinical dMRI acquisitions), map all parameters (cf. Supplementary Fig. S3a,b), and plot histograms for its both branches $\{f, D_a, D_e^{\parallel}, D_e^{\perp}, p_2\}_{\zeta=\pm}$ (red and blue dotted lines in Fig. 3) in white matter (WM, $\sim 11,000$ voxels), and in gray matter (GM, $\sim 13,000$ voxels), selected using probability masks. (WM mask was further thresholded by FA > 0.4 to exclude partial volume effects.)

We then use pairs of LEMONADE solutions with $\zeta = \pm$ in each voxel to initialize the full gradient-descent RotInv minimization (6), for which all the data with $b \leq 10$ is used (cf. Fig. S3c,d). This leads to the corresponding shaded histograms in Fig. 3. We can see that the output of full optimization (6) is qualitatively similar to that based on the Taylor expansion (3), with bimodal parameter histograms corresponding to the fundamental degeneracy of the parameter landscape corresponding to the two distinct branches of solutions.

Our analysis shows that the two branches are qualitatively distinct in the following ways: $f_+ > f_-$; also, usually, $D_a > D_e^{\parallel}$ for $\zeta = +$ and $D_a < D_e^{\parallel}$ for $\zeta = -$ (cf. equation (7) below). Generally, neither solution can be discarded based on parameter values alone, as they often fall within plausible biophysical bounds $0 < D \lesssim 3$ and $0 < f < 1$. Supplementary Fig. S4 shows that improvement in accuracy gained by nonlinear minimization (6) relative to LEMONADE occurs because small errors in estimated moments in the finite range of b translate into greater errors in the LEMONADE solutions, mostly due to errors in estimating the moment tensor $M^{(6)}$.

Branch index ζ in terms of ground truth parameters. Our analysis in Fig. 3 and in Supplementary Fig. S3 (cf. branch column) highlights the *stability of the branch index* ζ: The exact bimodality, following from the topology of minimization landscape at low-b, still affects parameter estimation even at very high b. Hence, branch assignment is akin to a discrete topological index, characterizing which part of the parameter space a given imaging voxel belongs to, based on its ground truth values.

In *Methods* we derive that the choice of the $\zeta = +$ branch corresponds to the ratio β between ground truth compartment diffusivities falling within the interval

$$4 - \sqrt{\tfrac{40}{3}} < \beta < 4 + \sqrt{\tfrac{40}{3}}\,, \quad \beta = \frac{D_a - D_e^{\parallel}}{D_e^{\perp}}\,, \qquad (7)$$

and the $\zeta = -$ branch should be chosen otherwise.

Branch choice is nontrivial because we *a priori* do not know the ground truth values D_a, $D_e^{\parallel}$ and $D_e^{\perp}$ entering equation (7); besides, these values may generally vary in different brain regions and be altered in pathology. Noise may affect estimated diffusivities enough to switch the estimated branch ratio β (Figs. 3 and S4), especially due to the division by small and particularly imprecise $D_e^{\perp}$.

Branch selection based on high b human data. Sensitivity to $\mathcal{O}(b^3)$ terms and beyond, ideally, will determine which branch $\zeta = \pm$ is the correct one, as well as the true minimum

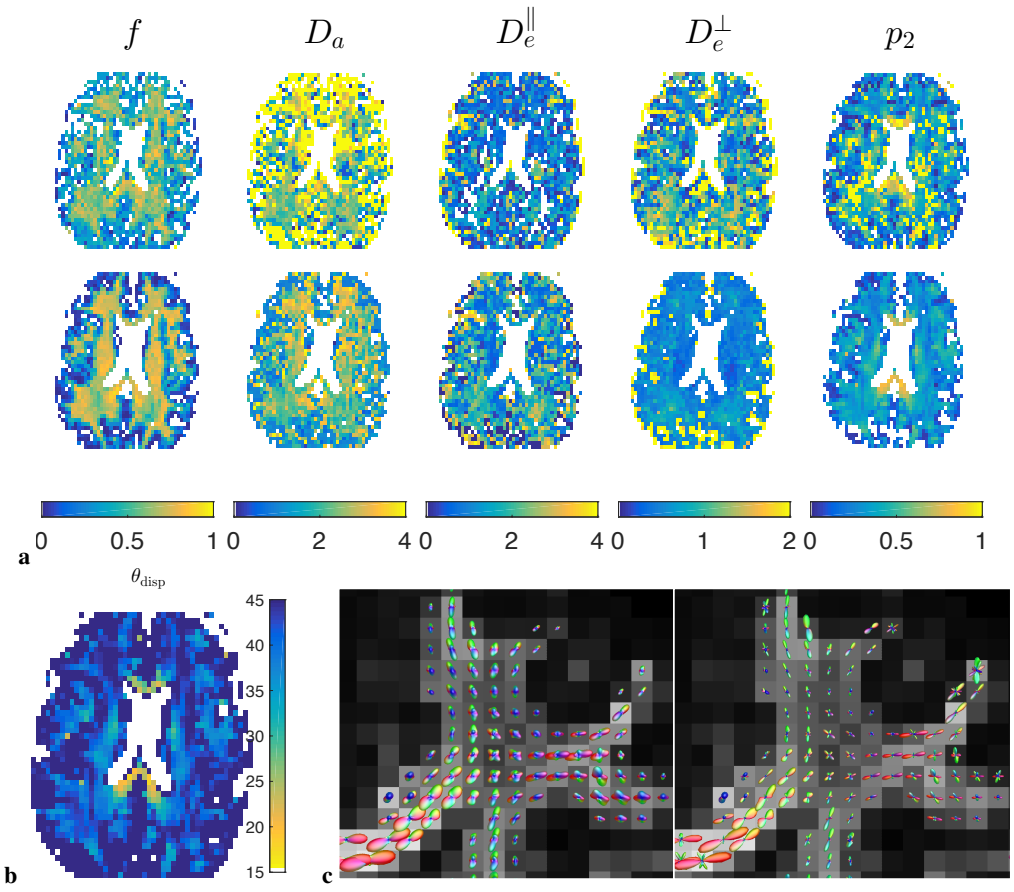


FIG. 4. **Scalar parameter maps and ODFs. a,** Maps calculated for subject 1 based on combining the outcomes of RotInv fitting (6). Top row: including only shells with $b \leq 2.5$, mimicking a clinically feasible acquisition, with branch selection according to $\zeta = +/-$ in WM/GM. Bottom row: prevalence maps for full b range. **b,** Fiber orientation dispersion angle θ_{disp} from p_2 (prevalence method) emphasizes major WM tracts. **c,** Empirical signal ODF (left, see text), and the fiber ODF calculated using p_{lm} from equation (5) (right), for the $b = 5$ shell, with $l \leq l_{\max} = 6$. Note the strong ODF sharpening effect, due to the deconvolution with locally estimated kernels $K_l(b)$.

(solution) along this branch. Practically, however, branch selection from realistic noisy data turns out to be quite challenging. Relying on very large b data is also tricky: the scaling[21] $S \sim f/\sqrt{bD_a}$ for $bD_a \gg 1$ is similar for both branches, since $f_+ > f_-$ and $D_{a+} > D_{a-}$, compensating each other's effect.

For now, to get the best available proxy for the ground truth, and to select the branch, we used our unique wide-b-range dedicated dMRI acquisition and calculate the scalar parameters independently of the branch location, solely based on the *prevalence*. In order to not bias our outcome on the branch choice, for each voxel, we initialize the problem (6) using 20 random starting points within the biophysically plausible parameter range (such as $0 < f, p_2 < 1$, and $0 < D < 3$ for all diffusivities), observe that the fit outcomes typically cluster around a few points in the parameter space, and select the predominant cluster (after excluding the outcomes outside the plausible bounds). An increasing b-range broadens the basin of attraction of the true minimum in a model calculation.[20] Supplementary Fig. S4 justifies this method using simulations for a range of ground truth values with added noise. Certainly, this method may still fail in some voxels, but the overall maps (Fig. 4) look sufficiently smooth and biophysically plausible. We performed the prevalence calculation for all three subjects and observed that the prevalence maps are similar.

Histograms of branch ratio (7) in Fig. 3 suggest that the $\zeta = +$ branch dominates in WM while $\zeta = -$ branch prevails in GM. There is a cluster of voxels with $D_a \approx D_e^{\parallel}$ such that $\beta \approx 4 - \sqrt{40/3} \approx 0.35$ (cf. also Fig. 5b); for those, branches merge since the discriminant $\mathcal{D} \to 0$, equation (24), and both estimated parameter sets coincide. There is recent evidence that $D_a \approx D_e^{\parallel}$ in rat spinal cord[28]. Overall, it remains an open question whether and by how much D_a and $D_e^{\parallel}$ differ[10,19,20,26]. Dedicated validation methods using "orthogonal" measurements[28–31] are warranted.

Maps from a clinically feasible acquisition, calculated with branch selection according to $\zeta = +/-$ in WM/GM, are shown in Fig. 4 (see Supplementary Fig. S3 for all processing steps). Fiber ODFs in Fig. 4, calculated using factorization relation (4), are notably sharper than empirical signal ODFs (calculated using SH coefficients $p_{lm}^{\mathrm{signal}} = (-)^{l/2} S_{lm}$ to align signal and fiber directions), since dividing by the locally estimated kernel $K_l(b)$ gives larger weight to the higher-order spherical harmonics. Small spurious ODF peaks are due to

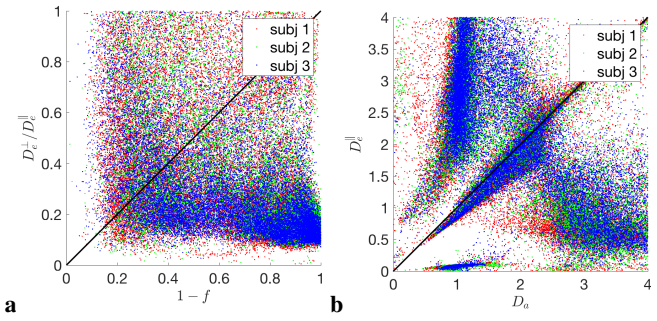


FIG. 5. **Are the scalar parameters independent?** To see whether we can rely on relations between scalar parameters in order to increase precision in their estimation, we investigate the validity of widely used constraints[10,19,26] using parameter values estimated from the prevalence method. Generally, these constraints fail. Colors correspond to 3 subjects, with all WM+GM voxels shown.

cutoff in the q-space (S_{lm} estimation is unconstrained). Fiber ODFs, rather than empirical signal ODFs, are a better starting point for any fiber tracking algorithm, as physics of diffusion gets factored out. Furthermore, voxel-wise estimated $f, D_a, D_e^\parallel, D_e^\perp$ and p_{lm} can serve as a starting point for mesoscopic global fiber tracking[32] that can provide further regularization of problem (1)–(2) by correlating over adjacent voxels.

Discussion

The rotational invariant framework for the overarching model (1) generalizes previous models which constrained parameter values or ODF shape, reveals a highly nontrivial topology of the fitting landscape, explains its degeneracies, and associated issues with accuracy and precision in all modern quantitative approaches to dMRI-based neuroimaging.

We observe that scalar parameter values in Fig. 4 exhibit WM/GM contrast, with the T_2-weighted axonal water fraction f highest in major tracts, approaching $0.7-0.8$. The neurite fraction drops significantly in GM, which may be explained by different T_2 values in extra- and intra-neurite spaces, as well as due to water within cell bodies effectively adding to extra-neurite fraction[33], and possible water exchange.

Notably, all three diffusivities generally vary across brain; we also observe that D_a is estimated more precisely than $D_e^\parallel$ and $D_e^\perp$ (cf. Supplementary Fig. S4). Scatter plots in Fig. 5 confirm that D_a, $D_e^\parallel$ and $D_e^\perp$ should be estimated independently, since neither of the widely employed constraints $D_e^\parallel = D_e^\perp/(1-f)$ and $D_a = D_e^\parallel$,[10,19,26] together with $D_a = D_e^\parallel = 1.7$,[10,19] seem to be valid. Scalar parameters do not abruptly differ between corpus callosum and the crossing regions such as centrum semiovale, emphasizing that our approach is able to separate the spatially varying orientational dispersion $\mathcal{P}(\hat{\mathbf{n}})$ from the kernel $\mathcal{K}$. Conversely, p_2 drops significantly in WM crossing regions, as well as in GM. Typical fiber orientation dispersion angle $\theta_{\rm disp}$, calculated as $\cos^2\theta_{\rm disp} \equiv (2p_2+1)/3$, delineates major WM tracts in Fig. 4b; the values $\theta_{\rm disp} \approx 20^\circ$ in genu and splenium agree remarkably well with the range $14^\circ - 22^\circ$ observed recently from NAA diffusion and from histology in human corpus callosum[34]. Even stronger orientational dispersion occurs in other WM regions, stressing the need to account for it[10,12,19].

While results in Fig. 3 favor branch selection $\zeta = \pm$ for WM/GM, our analysis formulates branch selection as an essential problem for quantifying neuronal microstructure, to be ultimately validated using very strong diffusion gradients (e.g. employing unique *Human Connectom* scanners with gradients up to 300 mT/m), as well as "orthogonal" acquisitions such as extra-neurite water suppression by strong gradients[28] and isotropic diffusion weighting[29–31]. The latter, yielding $S/S(0) = fe^{-bD_a} + (1-f)e^{-b(D_e^\parallel + 2D_e^\perp)}$, seems to produce relations $D_a \approx D_e^\parallel + 2D_e^\perp$ due to a relatively small iso-weighted kurtosis[29]. While this can be interpreted as favoring the $\zeta = +$ branch, this relation cannot be used as a global constraint: ref.[30] shows it failing in thalamus, apparently consistent with the $\zeta = -$ selection in GM (note however that thalamus is a GM/WM mixture). It is also interesting to further investigate the branch-merging case of $D_a \approx D_e^\parallel$.[28]

Unconstrained fit, equation (6), yields maps which for some parameters are quite noisy which may result in unphysical values (masked). Here we understand this as a general feature of the multicompartmental diffusion kernel (2) for any ODF, leading to the "trenches" in the landscape, Fig. 2. At this time, we are not aware of relations between parameters able to constrain the problem without introducing bias. Precision improvement can come from "orthogonal" measurements[29–31] cutting through the trenches, as well as from searching for solutions within the physical parameter ranges (e.g. by creating libraries of $K_l(b,x)$). This should be a subject of future work.

Generalizing, for any number of compartments in the kernel (2), scalar parameters can be determined from a set (5) of basis-independent rotational invariants. Branch-selection degeneracy of the scalar sector will persist for 3 or more compartments. Relating invariant moments (3) to kernel parameters can be used to analyze this degeneracy. If the added compartment(s) are isotropic, the LEMONADE branches will correspond to the anisotropic 2-compartment part of the kernel $\mathcal{K}$, determining the respective higher-dimensional "low-energy" manifolds in parameter space. Methods other than gradient descent (e.g. library-based or Bayesian[35], based on similar invariants) can be utilized for solving system (5); applicability of all such methods hinges on resolving branch selection that determines the biophysically correct parameter domain.

Outlook

Using SO(3) symmetry and representation theory, we separated parameter estimation problem for neuronal microstructure into scalar and tensor (ODF) sectors. Taylor-expansion analysis of scalar sector reveals nontrivial topology of parameter landscape, with the first few moments exactly determining two narrow trenches along which the parameters approximate dMRI measurements almost equally well. This degeneracy is intrinsic to problem (1)–(2) with *any* ODF, revealing issues with accuracy precision in parameter estimation.

Branch selection criterion (7) determines the domain for the physical solution. The choice $\zeta = \pm$ for WM/GM remains to

be validated by estimating ground truth compartment diffusivity values in animal studies, and by using strong diffusion gradients or alternative acquisition schemes.

The combination of a linearized solution for the moments and the subsequent nonlinear optimization gives rise to an unconstrained algorithm for parametric maps in the whole brain, performing about 2 orders of magnitude faster than current methods employing constraints on kernel parameters, and on the ODF shape. Our analysis shows that commonly used constraints between the scalar parameters generally do not hold, and can severely bias the remaining parameters due to the nontrivial topology of the minimization landscape.

We believe our approach sets the stage for unbiased noninvasive clinically feasible mapping of key neuronal microstructure parameters orders of magnitude below MRI resolution, opening the window into architectural, orientational and functional changes in pathology, aging and development, and bridging the gap between biophysical modeling, basic neuroscience, and clinical MRI.

Methods

Factorization. Since kernel (2) is axially symmetric, it can be expanded in even-order Legendre polynomials $P_l(\xi)$ (i.e. in the $m = 0$ SHs), as function of $\xi \equiv \cos\theta$ (for given scalar parameters x):

$$\mathcal{K}(b,\xi) = \sum_{l=0,2,\ldots} (2l+1) K_l(b) P_l(\xi)\,, \tag{8}$$

$$K_l(b) \equiv \int_0^1 \mathrm{d}\xi\, \mathcal{K}(b,\xi) P_l(\xi)\,. \tag{9}$$

Applying the SH addition formula

$$P_l(\hat{\mathbf{g}}\cdot\hat{\mathbf{n}}) = \frac{4\pi}{2l+1} \sum_{m=-l}^{l} Y_{lm}(\hat{\mathbf{g}}) Y^*_{lm}(\hat{\mathbf{n}}) \tag{10}$$

yields equation (5) of the main text, where SH components S_{lm} (with even l only, due to $\hat{\mathbf{n}} \to -\hat{\mathbf{n}}$ symmetry) are defined in a standard way,

$$S_{\hat{\mathbf{g}}}(b) = \sum_{l=0,2,\ldots} \sum_{m=-l}^{l} S_{lm}(b) Y_{lm}(\hat{\mathbf{g}})\,. \tag{11}$$

Functions (9) were used by Jespersen *et al.*[5] for the full fitting (4).

Multiple minima: A toy model. To develop intuition about the problem (1)–(2), we first consider its simple variant that already has the main signatures of the general solution. Suppose we were able to measure the kernel $\mathcal{K}(b,\xi)$ directly — i.e. assume for a moment that an imaging voxel is small enough to contain only one fiber orientation $\hat{\mathbf{n}}$ — but our measurements were limited only to directions parallel ($\|$, $\xi = 1$) and transverse ($\perp$, $\xi = 0$) to the fascicle. Since typical human dMRI has $bD_i \sim 1$, where $D_i = \{D_a, D_e^{\|}, D_e^{\perp}\}$, fitting practically performs matching between the first few moments (Taylor coefficients) of the signal and of the series $\mathcal{K} \simeq 1 - bD + \frac{b^2}{2!}M - \ldots$. Matching up to $\mathcal{O}(b)$ and up to $\mathcal{O}(b^2)$ respectively yields

$$\begin{array}{rclcrcl} D^{\perp} &=& (1-f)D_e^{\perp}\,, & & D^{\|} &=& fD_a + (1-f)D_e^{\|}\,; \\ M^{\perp} &=& (1-f){D_e^{\perp}}^2\,, & & M^{\|} &=& f{D_a}^2 + (1-f){D_e^{\|}}^2\,. \end{array} \tag{12}$$

In $\perp$ direction, scalar parameters $D_e^{\perp} = M^{\perp}/D^{\perp}$ and $f = 1 - {D^{\perp}}^2/M^{\perp}$ are uniquely expressed via the moments. However, there are *two* possible solutions of the corresponding quadratic equation ${D_e^{\|}}^2 - 2D^{\|}\cdot D_e^{\|} + ({D^{\|}}^2 - fM^{\|})/(1-f) = 0$ for $D_e^{\|}$ (and hence, D_a) in $\|$ direction, cf. refs.[8,9]. The duality arises from choosing the $\zeta = \pm$ branch of the square root $D_{e,\zeta}^{\|} = D^{\|} + \zeta\sqrt{\mathcal{D}}$, where $\mathcal{D} = \frac{f}{1-f}\left(M^{\|} - {D^{\|}}^2\right)$. To understand which branch ζ to choose, let us express the discriminant $\mathcal{D}$ in terms of the original model parameters, using equations (12). Remarkably, $\mathcal{D} = f^2\left(D_a - D_e^{\|}\right)^2$ is a *full square*, such that $\sqrt{\mathcal{D}} = \eta f\left(D_a - D_e^{\|}\right)$, where $\eta = \mathrm{sgn}\left(D_a - D_e^{\|}\right)$.

With the above $\sqrt{\mathcal{D}}$, we get back the correct values $D_{e,\zeta}^{\|} = D_e^{\|}$ and $D_{a,\zeta} = D_a$ when $\zeta\eta = -1$. However, with the wrong branch choice $\zeta\eta = +1$, the apparent diffusivities differ from the true ones:

$$\begin{array}{rcl} {D_a}^{\mathrm{app}} &=& (2f-1)D_a + 2(1-f)D_e^{\|}\,, \\ {D_e^{\|}}^{\mathrm{app}} &=& 2fD_a + (1-2f)D_e^{\|}\,. \end{array} \tag{13}$$

Note that in this case, as expected, ${D_e^{\|}}^{\mathrm{app}} - {D_a}^{\mathrm{app}} = -\left(D_e^{\|} - D_a\right)$, i.e. the difference has the same absolute value and a wrong sign.

To recap, there exist two solutions of equations (12) which, up to $\mathcal{O}(b^2)$, exactly satisfy the toy parameter estimation problem. Hence, there will be two distinct minima in the toy "energy" function (analog of equation (6)), because of the branch selection ambiguity. This feature originates from the two-compartment nature of the model. It is the $\mathcal{O}(b^3)$ term that would elevate the wrong minimum above the true one. If noise overwhelms the $\mathcal{O}(b^3)$ effect, there will be no way to select the correct branch ζ based on comparing the values of the energy function in both minima[20]. Note that *wrong values (13) can be completely plausible*; in particular, for the symmetric case $f = 1/2$, the diffusivities are *swapped* — i.e. we mistake the intra- for the extra-axonal. We also see that the branch choice ζ depends on η, i.e. the $+$ branch should be selected if $D_a < D_e^{\|}$, and vice-versa. (For this toy example, branch choice is different from equation (7) because we involved components of $M^{(4),4m}$, in addition to $M^{(4),2m}$, and constrained $p_2 \equiv p_4 \equiv 1$. Qualitative issues are similar.)

Expansion in the moments. Parameter counting. Our goal is to extend the logic and intuition gained by Taylor-expanding the above toy model onto the general case (1). For that, let us first count the number of parameters of the moments expansion (3) as a function of the maximal even order $l_{\max}$. A term $M^{(l)}_{i_1\ldots i_l}$ of rank l is a fully symmetric tensor, which can be represented in terms of symmetric trace-free (STF) tensors of rank l, $l-2$, …, 2, 0. Each set of STF tensors realizes an irreducible representation of the SO(3) group of rotations, equivalent[36] to the set of $2l+1$ SH Y_{lm}. Truncating the series (3) at $l = l_{\max}$ means that we determine all components of $M^{(l)}_{i_1\ldots i_l}$ for $l = 0, 2, \ldots, l_{\max}$, with the total number of parameters

$$N_c(l_{\max}) = \sum_{l=2,4,\ldots}^{l_{\max}} n_c(l) = \frac{1}{12}\,l_{\max}^3 + \frac{5}{8}\,l_{\max}^2 + \frac{17}{12}\,l_{\max} \tag{14}$$

corresponding to $N_c = 6,\ 21,\ 49, \ldots$ for $l_{\max} = 2,\ 4,\ 6, \ldots$. (Here $n_c(l)$ is given after equation (3); assuming normalization $S(0) \equiv 1$ in equation (3), we did not include the unweighted signal in our counting). Equation (14) counts the numbers of DTI, DKI, etc components, which can be determined linearly (hence, robustly and quickly) from the measurement, using the b-matrix pseudoinversion.

Comparing $N_c(l_{\max})$ with the corresponding number of model parameters $N_p(l_{\max})$ determined after equation (3), it naively looks like the series (3) is overdetermined, $N_c \geq N_p$, already for $l_{\max} \geq 4$. In what follows we will see that all model parameters can be determined from the series (3) only starting from $l_{\max} \geq 6$, which is a very important practical limitation for the parameter estimation. As mentioned in the main text, it turns out that for $l_{\max} = 4$, there are not enough equations for scalar model parameters, and too many for the tensor parameters p_{lm}.

To connect the moments to the model parameters, and to explore the low-energy landscape of the problem (6), let us expand the signal (1). The $\mathcal{O}(b)$ term, $l=2$, yields the diffusion tensor

$$M^{(2)}_{ij} = fD_a \langle n_i n_j\rangle + (1-f)\left(D_e^\perp \delta_{ij} + \Delta_e \langle n_i n_j\rangle\right) \quad (15a)$$

where $\langle n_i n_j\rangle = \int \mathrm{d}\hat{\mathbf{n}}\, \mathcal{P}(\hat{\mathbf{n}})\, n_i n_j$ and

$$\Delta_e \equiv D_e^\parallel - D_e^\perp \,.$$

Expanding (1) up to $\mathcal{O}(b^2)$ and $\mathcal{O}(b^3)$ yields the 4$^{\text{th}}$ and 6$^{\text{th}}$ order moments

$$\begin{aligned} M^{(4)}_{ijkl} &= f{D_a}^2 \langle n_i n_j n_k n_l\rangle + (1-f)\Big[{D_e^\perp}^2 \delta_{(ij}\delta_{kl)} \\ &\quad + 2D_e^\perp \Delta_e \langle n_{(i} n_j\rangle \delta_{kl)} + {\Delta_e}^2 \langle n_i n_j n_k n_l\rangle\Big]\,; \quad (15b) \\ M^{(6)}_{i_1\ldots i_6} &= f{D_a}^3 \langle n_{i_1}\ldots n_{i_6}\rangle + (1-f)\Big[{D_e^\perp}^3 \delta_{(i_1 i_2}\delta_{i_3 i_4}\delta_{i_5 i_6)} \\ &\quad + 3{D_e^\perp}^2 \Delta_e \delta_{(i_1 i_2}\delta_{i_3 i_4}\langle n_{i_5} n_{i_6)}\rangle \quad (15c) \\ &\quad + 3D_e^\perp {\Delta_e}^2 \delta_{(i_1 i_2}\langle n_{i_3}\ldots n_{i_6)}\rangle + {\Delta_e}^3 \langle n_{i_1}\ldots n_{i_6}\rangle\Big]\,. \end{aligned}$$

Here symmetrization[36] over tensor indices between $_{(\ldots)}$ is assumed:

$$\begin{aligned} \delta_{(ij}\delta_{kl)} &= \tfrac{1}{3}\left(\delta_{ij}\delta_{kl} + \delta_{ik}\delta_{jl} + \delta_{il}\delta_{jk}\right), \\ \langle n_{(i} n_j\rangle \delta_{kl)} &= \tfrac{1}{6}\left[\langle n_i n_j\rangle\delta_{kl} + \langle n_i n_k\rangle\delta_{jl} + \langle n_i n_l\rangle\delta_{jk}\right. \\ &\quad \left. + \langle n_k n_l\rangle\delta_{ij} + \langle n_j n_l\rangle\delta_{ik} + \langle n_j n_k\rangle\delta_{il}\right], \end{aligned}$$

such that $\delta_{(ij}\delta_{kl)} g_i g_j g_k g_l = 1$, $\langle n_{(i} n_j\rangle \delta_{kl)} g_i g_j g_k g_l = \langle n_i n_j\rangle g_i g_j$. Similarly, symmetrized tensors in equation (15c), when convolved with $g_{i_1}\ldots g_{i_6}$, yield the corresponding powers of the product $\hat{\mathbf{g}}\cdot\hat{\mathbf{n}}$.

In principle, one can proceed further, with the escalating complexity of relating the higher-order moments of the signal to the nonlinear combinations of the scalar model parameters $x = \{f, D_a, D_e^\parallel, D_e^\perp\}$ and of the ODF averages $\langle n_{i_1}\ldots n_{i_l}\rangle \equiv \int \mathrm{d}\hat{\mathbf{n}}\, \mathcal{P}(\hat{\mathbf{n}})\, n_{i_1}\ldots n_{i_l}$. We would like to *invert* the above relations: to solve for the ODF expansion parameters p_{lm} and the scalar parameters x in terms of the moments $M^{(l)}_{i_1\ldots i_l}$, and to explore the properties of the solution.

Scalar-tensor factorization for the moments: LEMONADE. The 49 equations (15) provide an overdetermined nonlinear system for 31 model parameters. To obtain an exact solution of this system we will utilize symmetry, by working in the irreducible representations of the SO(3) group, for which this challenging problem factorizes. The SO(3) representations in equations (15) are selected by projecting the products $n_{i_1}\ldots n_{i_l}$ onto the special STF tensors $\mathcal{Y}^{lm}_{k_1\ldots k_l}$, defined in equation (2.11) of ref.[36], that generate SHs

$$Y_{lm}(\hat{\mathbf{n}}) = \mathcal{Y}^{lm}_{k_1\ldots k_l} n_{k_1}\ldots n_{k_l}\,. \quad (16)$$

(Since ODF is real, here we re-define $\mathcal{Y}^{lm}_{k_1\ldots k_l} \to \sqrt{2}\,\mathrm{Re}\,\mathcal{Y}^{lm}_{k_1\ldots k_l}$ for $m>0$ and $\mathcal{Y}^{lm}_{k_1\ldots k_l} \to \sqrt{2}\,\mathrm{Im}\,\mathcal{Y}^{l|m|}_{k_1\ldots k_l}$ for $m<0$, to work in real SH basis.) Introducing the corresponding moments in the SH basis

$$M^{(L),lm} = \frac{4\pi}{\mathcal{N}_l}\,\mathcal{Y}^{lm}_{k_1\ldots k_l}\delta_{k_{l+1}k_{l+2}}\ldots\delta_{k_{L-1}k_L}\,M^{(L)}_{k_1\ldots k_L}\,, \quad (17)$$

we relate $M^{(L),lm}$ to the model parameters by convolving equations (15) with $\mathcal{Y}^{lm}_{k_1\ldots k_l}\delta_{k_{l+1}k_{l+2}}\ldots\delta_{k_{L-1}k_L}$, and by using the following identities, which can be proven by direct inspection, for $L=4$

$$\begin{aligned} \delta_{(ij}\delta_{kl)}\delta_{kl} &= \tfrac{5}{3}\,\delta_{ij}\,, \quad \delta_{(ij}\delta_{kl)}\delta_{ij}\delta_{kl} = 5\,; \\ \langle n_{(i} n_j\rangle\delta_{kl)}\delta_{kl} &= \tfrac{1}{6}\left[7\langle n_i n_j\rangle + \delta_{ij}\right], \quad \langle n_{(i} n_j\rangle\delta_{kl)}\delta_{ij}\delta_{kl} = \tfrac{5}{3}\,; \end{aligned}$$

and for $L=6$:

$$\begin{aligned} \delta_{(i_1 i_2}\ldots\delta_{i_5 i_6)}\delta_{i_1 i_2}\delta_{i_3 i_4}\delta_{i_5 i_6} &= 7\,, \\ \delta_{(i_1 i_2}\delta_{i_3 i_4}\langle n_{i_5} n_{i_6)}\rangle\delta_{i_1 i_2}\delta_{i_3 i_4}\delta_{i_5 i_6} &= \tfrac{7}{3}\,, \\ \delta_{(i_1 i_2}\langle n_{i_3}\ldots n_{i_6)}\rangle\delta_{i_1 i_2}\delta_{i_3 i_4}\delta_{i_5 i_6} &= \tfrac{7}{5}\,. \end{aligned}$$

As a result, we obtain the minimal system for $L\le 6$ and $l=0,2$:

$$M^{(2),00} = fD_a + (1-f)(3D_e^\perp + \Delta_e) \quad (18a)$$

$$\frac{M^{(2),2m}}{p_{2m}/\mathcal{N}_2} = fD_a + (1-f)\Delta_e \quad (18b)$$

$$M^{(4),00} = f{D_a}^2 + (1-f)\left[5{D_e^\perp}^2 + \frac{10}{3}D_e^\perp\Delta_e + {\Delta_e}^2\right] \quad (18c)$$

$$\frac{M^{(4),2m}}{p_{2m}/\mathcal{N}_2} = f{D_a}^2 + (1-f)\left[\frac{7}{3}D_e^\perp\Delta_e + {\Delta_e}^2\right] \quad (18d)$$

$$\begin{aligned} M^{(6),00} &= f{D_a}^3 \\ &\quad + (1-f)\left[7{D_e^\perp}^2(D_e^\perp + \Delta_e) + \frac{21}{5}D_e^\perp{\Delta_e}^2 + {\Delta_e}^3\right] \end{aligned} \quad (18e)$$

$$\frac{M^{(6),2m}}{p_{2m}/\mathcal{N}_2} = f{D_a}^3 + (1-f)\left[\frac{21}{5}{D_e^\perp}^2\Delta_e + \frac{18}{5}D_e^\perp{\Delta_e}^2 + {\Delta_e}^3\right] \quad (18f)$$

The system (18) involves minimal orders L and l enough to find all the 4 scalar kernel parameters x and p_2. Indeed, by defining $M^{(l),2} \equiv ||M^{(l),2m}||$, and p_2 as defined before equation (5), we get the same system as (18) but with $M^{(l),2}/p_2$ in the left-hand side of equations (18b), (18d) and (18f). The above system has 6 equations for 5 parameters; even if we added the CSF compartment with its fraction and an isotropic $D_{\text{CSF}} = 3\,\mu\text{m}^2/\text{ms}$, we could in principle still determine the 6 parameters from appropriately modified system (18). Having found the parameters of the kernel (2), equation

$$M^{(l),lm} = \frac{p_{lm}}{\mathcal{N}_l}\cdot\left[f{D_a}^{l/2} + (1-f){\Delta_e}^{l/2}\right] \quad (18g)$$

yields the ODF parameters p_{lm} up to *arbitrary* order $l\le l_{\max}$, as long as $M^{(l),lm}$ are linearly found from series (3) and equation (17). Equations (18) are equivalent to matching the Taylor expansion of equation (4), and to minimizing the expanded energy (6).

We call the exact relations (18) between the signal's moments $M^{(L),lm}$ in the SH basis, and the model parameters f, D_a, $D_e^\parallel$, Δ_e and p_{lm}, LEMONADE (Linearly Estimated Moments provide Orientations of Neurites And their Diffusivities Exactly). Throughout this work, we consider the rotationally invariant form of system (18), with $M^{(l),2}/p_2$, $l=2,4,6$, in the left-hand side of equations (18b), (18d) and (18f), correspondingly.

LEMONADE exact solutions: Low-energy branches. To solve the system (18), we first focus on equations (18a)–(18d), and eliminate D_a, $D_e^\perp$ and Δ_e. Introducing the common scaling factor

$$\bar{D}(p_2) \equiv \tfrac{1}{3}\left(M^{(2),00} - M^{(2),2}/p_2\right) = (1-f)D_e^\perp\,, \quad (19)$$

we make all quantities dimensionless functions of p_2 and f:

$$\begin{aligned} d_a &\equiv \frac{D_a}{\bar{D}}\,, \quad d_2 \equiv \frac{M^{(2),2}}{p_2\bar{D}}\,, \quad \delta_e \equiv \frac{\Delta_e}{\bar{D}} = \frac{d_2 - f d_a}{1-f}\,, \\ m_0 &\equiv \frac{M^{(4),00}}{\bar{D}^2}\,, \quad m_2 \equiv \frac{M^{(4),2}}{p_2\bar{D}^2}\,, \quad d_e^\perp \equiv \frac{D_e^\perp}{\bar{D}} = \frac{1}{1-f}\,, \end{aligned} \quad (20)$$

such that moments d_2, m_0, m_2 are functions of p_2 and $f = f(p_2)$:

$$\Delta m(p_2) \equiv m_0 - m_2 = 5d_e^\perp + \delta_e = \frac{5 + d_2 - f d_a}{1-f}\,. \quad (21)$$

Multiplying the dimensionless equation (18d) by f,

$$fm_2 = (fd_a)^2 + f(d_2 - fd_a)\left[\frac{7}{3}\frac{1}{1-f} + \frac{d_2 - fd_a}{1-f}\right]$$

and eliminating d_a using equation (21), the f^3 term fortuitously cancels, and we are left with a *quadratic* equation

$$af^2 - \left(a + c - \tfrac{40}{3}\right)f + c = 0\,, \tag{22}$$

where the functions $a = a(p_2)$ and $c = c(p_2)$ are given by

$$a = (\Delta m)^2 - \left(\tfrac{7}{3} + 2d_2\right)\Delta m + m_2\,, \quad c = (\Delta m - 5 - d_2)^2\,. \tag{23}$$

We observe that, similar to the toy model (12) above, the full LEMONADE system (18) up to $\mathcal{O}(b^2)$ yields *two* possible solutions $f = f_\pm(p_2)$, corresponding to the two branches of $\sqrt{\mathcal{D}}$. Here, the discriminant of equation (22), expressed via the original parameters, using $c = f^2/(1-f)^2 \cdot (5 + d_2 - d_a)^2$ and $a = c/f + \frac{40}{3}/(1-f)$, is again a *full square*

$$\mathcal{D} = \left(a - c - \tfrac{40}{3}\right)^2 - \tfrac{160}{4}\,c \equiv \left(\tfrac{f}{1-f}\right)^2\left[\left(5 + d_2 - d_a\right)^2 - \tfrac{40}{3}\right]^2, \tag{24}$$

such that $\sqrt{D} = \eta \cdot \frac{f}{1-f}\left[\left(5 + d_2 - d_a\right)^2 - \frac{40}{3}\right]$, and the sign η of the expression in the $[\ldots]$ bracket is defined as

$$\eta \equiv \operatorname{sgn}\left(|\beta - 4| - \sqrt{\tfrac{40}{3}}\right), \quad \beta = \frac{D_a - D_e^\parallel}{D_e^\perp}\,. \tag{25}$$

Here we used that $5 + d_2 - d_a = 4 + \left(D_e^\parallel - D_a\right)/D_e^\perp$ in terms of the original model parameters, independent of f. Similar to the branch selection for the toy model (12), after expressing a and c in terms of the original model parameters, the correct solution $f_\zeta \equiv f$ corresponds to $\zeta\eta = -1$ sign choice for selecting the $\pm\sqrt{\mathcal{D}}$ term in the branch

$$f_\zeta(p_2) = \left(a + c - \tfrac{40}{3} + \zeta\sqrt{\mathcal{D}}\right)/2a\,, \tag{26}$$

equivalent to the branch selection (7) in the main text. Choosing the opposite branch will, roughly, swap the compartment diffusivity values, similar to the toy model (12) considered in detail above.

An important difference of the general solution (26) from the toy model (12) is the remaining dependence on p_2, due to the arbitrary fiber ODF, leaving the model parameters undetermined at $\mathcal{O}(b^2)$: the branches $f_\pm(p_2)$ correspond to the *two 1-dimensional manifolds* of model parameters $\{f(p_2),\, D_a(p_2),\, D_e^\parallel(p_2),\, D_e^\perp(p_2),\, p_2\}_\pm$ which exactly satisfy the first 4 equations of the system (18). These manifolds correspond to the two trenches in the low-energy landscape of the full RotInv problem (6), Fig. 2 and Figs. S1–S2, which are flat if our acquisition is only sensitive to $\mathcal{O}(b^2)$. It is the $\mathcal{O}(b^3)$ terms, corresponding to equations (18e) and (18f), that in the noise-free case select the correct trench (elevating F for the wrong one), and yield the value p_2 fixing the minimum of F in the correct trench.

As long as the branch index ζ is known, substitution of equation (26) into the two (overdetermined) equations (18e) and (18f) yields p_2 and hence all scalar model parameters. The numerical solution is fastest ($\sim$ 1 millisecond/voxel on a desktop computer) by simply performing exhaustive search for the arg min of the sum of squares of equations (18e) and (18f) on the discretized interval $0 \le p_2 \le 1$.

Estimating moments. We estimate cumulant tensors $C^{(l)}$

$$\ln\frac{S_{\hat{\mathbf{g}}}(b)}{S(0)} = -bC^{(2)}_{i_1 i_2} g_{i_1} g_{i_2} + b^2 C^{(4)}_{i_1\ldots i_4} g_{i_1}\ldots g_{i_4} - \ldots \tag{27}$$

and $S(0)$, via linear matrix pseudoinversion of $\ln S_{\hat{\mathbf{g}}}(b)$ with voxel-specific weights[37] up to $l_{\max} = 6$. We then convert $C^{(l)}_{i_1\ldots i_l}$ to the moments $M^{(l)}_{i_1\ldots i_l}$ in a standard way[38], by adding the reducible parts from lower-order $C^{(l)}$. For unbiased estimation, we use only shells within $0 \le b \le 2.5$, where the cumulant series converges.

Implementation and computation time. Processing steps were implemented in *Matlab* (MathWorks, Natick, MA, USA), according to equations (27) and (18)–(26) using standard library functions, and the Levenberg-Marquardt algorithm for nonlinear minimization of equation (6). For the whole brain (34383 voxels within the WM+GM mask for subject 1) on a desktop iMac (4 cores), it took under 2 min for estimating the cumulants using the b-matrix pseudoinversion with the voxel-specific weights[37], together with recalculating the moments $M^{(L),lm}$ from the cumulants (only the range $b \le 2.5$ was used for unbiased estimation); 1.5 min for LEMONADE calculation (both branches); and 5-15 min for nonlinear fitting (both branches for all voxels, for $b \le 10$ and $b \le 2.5$ respectively), using the corresponding LEMONADE solutions as fit initialization. Nonlinear fitting achieves considerable speedup because of the initial values being already quite close to the minima of F; we also precomputed corresponding integrals (9) and their first derivatives in a broad range.

MRI. Three healthy volunteers underwent imaging on a Siemens Prisma 3T whole-body MRI scanner. The study was approved by the local Institutional Review Board, and informed consent was obtained and documented from all participants. The MRI scanner was equipped with a $80\,\mathrm{mT/m}$ gradient system and a 64-channel receiver head coil. The body coil was used for transmission. A monopolar diffusion-weighted EPI sequence was used to acquire the dMRI data. Diffusion weighting was applied along 64 isotropically distributed gradient directions for each of the 21 b-values that were equidistantly distributed in the range $[0 : 0.5 : 10]\,\mathrm{ms/\mu m^2}$. Following imaging parameters were kept constant throughout the data acquisition sequence: $\mathrm{TR/TE} : 4000/105\,\mathrm{ms}$, matrix: 80×80, NEX: 1, in-plane resolution: $3 \times 3\,\mathrm{mm}^2$, slice thickness: $3\,\mathrm{mm}$, slices: 38, parallel imaging: GRAPPA with acceleration factor 2, reconstructed using the adaptive combine algorithm to ensure Rician data distribution, multiband acceleration with factor 2, and no partial Fourier.

Image processing. MP-PCA noise estimation and denoising method[39] allowed us to preserve only the significant principal components and to strongly reduce the noise in the data and to estimate spatially varying noise map. The positive signal bias, inherent to low-SNR magnitude MR data, was removed by using the method of moments[40], where the denoised signal was used as a proxy for the Rician expectation value. Denoised and Rice-floor-corrected images were subsequently corrected for Gibbs ringing[41,42], geometric eddy current distortions and subject motion[43].

Acknowledgments. This work has benefited from fruitful discussions with Marco Reisert, Valerij Kiselev, Bibek Dhital and Elias Kellner. Research was supported by the Fellowship from Raymond and Beverly Sackler Laboratories for Convergence of Physical, Engineering and Biomedical Sciences, by the Litwin Foundation for Alzheimer's Research, and by the National Institute of Neurological Disorders and Stroke of the NIH under award number R01NS088040. JV is a Postdoctoral Fellow of the Research Foundation – Flanders (FWO; grant number 12S1615N). Photo credit to Tom Deerinck and Mark Ellisman (National Center for Microscopy and Imaging Research) for the histology image illustrating a fiber fascicle in Fig. 1.

Author contributions. DSN, JV, IOJ and EF planned experiments. IOJ and EF performed experiments. DSN, JV and IOJ performed data analysis. DSN performed analytical calculations and wrote the paper. All authors discussed the results and implications and commented on the manuscript at all stages.

* dima@alum.mit.edu

[1] C. Beaulieu, "The basis of anisotropic water diffusion in the nervous system - a technical review," NMR in Biomedicine **15**, 435–455 (2002).

[2] Derek K Jones, *Diffusion MRI: Theory, Methods, and Applications* (Oxford University Press, New York, 2011).

[3] TEJ Behrens, H Johansen-Berg, MW Woolrich, SM Smith, CAM Wheeler-Kingshott, PA Boulby, GJ Barker, EL Sillery, K Sheehan, O Ciccarelli, *et al.*, "Non-invasive mapping of connections between human thalamus and cortex using diffusion imaging," Nature Neuroscience **6**, 750–757 (2003).

[4] Christopher D Kroenke, Joseph J H Ackerman, and Dmitriy A Yablonskiy, "On the nature of the NAA diffusion attenuated MR signal in the central nervous system," Magn Reson Med **52**, 1052–9 (2004).

[5] Sune N. Jespersen, Christopher D. Kroenke, Leif Ostergaard, Joseph J. H. Ackerman, and Dmitriy A. Yablonskiy, "Modeling dendrite density from magnetic resonance diffusion measurements," Neuroimage **34**, 1473–1486 (2007).

[6] Sune N. Jespersen, Carsten R. Bjarkam, Jens R. Nyengaard, M. Mallar Chakravarty, Brian Hansen, Thomas Vosegaard, Leif Ostergaard, Dmitriy Yablonskiy, Niels Chr. Nielsen, and Peter Vestergaard-Poulsen, "Neurite density from magnetic resonance diffusion measurements at ultrahigh field: Comparison with light microscopy and electron microscopy," Neuroimage **49**, 205–216 (2010).

[7] Y Assaf, R Z Freidlin, G K Rohde, and P J Basser, "New modeling and experimental framework to characterize hindered and restricted water diffusion in brain white matter," Magnetic Resonance In Medicine **52**, 965–978 (2004).

[8] Els Fieremans, Dmitry S. Novikov, Jens H. Jensen, and Joseph A. Helpern, "Monte Carlo study of a two-compartment exchange model of diffusion," NMR in Biomedicine **23**, 711–724 (2010).

[9] Els Fieremans, Jens H Jensen, and Joseph A Helpern, "White matter characterization with diffusional kurtosis imaging," Neuroimage **58**, 177–88 (2011).

[10] Hui Zhang, Torben Schneider, Claudia A Wheeler-Kingshott, and Daniel C Alexander, "NODDI: practical in vivo neurite orientation dispersion and density imaging of the human brain," Neuroimage **61**, 1000–16 (2012).

[11] Stamatios N Sotiropoulos, Timothy EJ Behrens, and Saad Jbabdi, "Ball and rackets: inferring fiber fanning from diffusion-weighted mri," NeuroImage **60**, 1412–1425 (2012).

[12] Uran Ferizi, Torben Schneider, Thomas Witzel, Lawrence L Wald, Hui Zhang, Claudia A M Wheeler-Kingshott, and Daniel C Alexander, "White matter compartment models for in vivo diffusion mri at 300mt/m," Neuroimage **118**, 468–83 (2015).

[13] Dmitry S Novikov, Jens H Jensen, Joseph A Helpern, and Els Fieremans, "Revealing mesoscopic structural universality with diffusion," Proc Natl Acad Sci U S A **111**, 5088–93 (2014).

[14] Lauren M Burcaw, Els Fieremans, and Dmitry S Novikov, "Mesoscopic structure of neuronal tracts from time-dependent diffusion," NeuroImage **114**, 18–37 (2015).

[15] Els Fieremans, Lauren M Burcaw, Hong-Hsi Lee, Gregory Lemberskiy, Jelle Veraart, and Dmitry S Novikov, "In vivo observation and biophysical interpretation of time-dependent diffusion in human white matter," NeuroImage (2016).

[16] Els Fieremans, Jens H. Jensen, Joseph A. Helpern, Sungheon Kim, Robert I. Grossman, Matilde Inglese, and Dmitry S. Novikov, "Diffusion distinguishes between axonal loss and demyelination in brain white matter," Proceedings of the International Society of Magnetic Resonance in Medicine 20, p.714 (2012).

[17] Ileana O Jelescu, Magdalena Zurek, Kerryanne V Winters, Jelle Veraart, Anjali Rajaratnam, Nathanael S Kim, James S Babb, Timothy M Shepherd, Dmitry S Novikov, Sungheon G Kim, and Els Fieremans, "In vivo quantification of demyelination and recovery using compartment-specific diffusion mri metrics validated by electron microscopy," Neuroimage **132**, 104–14 (2016).

[18] Matthew D. Budde and Joseph A. Frank, "Neurite beading is sufficient to decrease the apparent diffusion coefficient after ischemic stroke," Proceedings of the National Academy of Sciences of the United States of America **107**, 14472–14477 (2010).

[19] Maira Tariq, Torben Schneider, Daniel C Alexander, Claudia A Gandini Wheeler-Kingshott, and Hui Zhang, "Bingham–noddi: Mapping anisotropic orientation dispersion of neurites using diffusion mri," NeuroImage (2016).

[20] Ileana O Jelescu, Jelle Veraart, Els Fieremans, and Dmitry S Novikov, "Degeneracy in model parameter estimation for multi-compartmental diffusion in neuronal tissue," NMR in Biomedicine **29**, 33–47 (2016).

[21] Jens H Jensen, G Russell Glenn, and Joseph A Helpern, "Fiber ball imaging," NeuroImage **124**, 824–833 (2016).

[22] Jens H Jensen, Joseph A Helpern, Anita Ramani, Hanzhang Lu, and Kyle Kaczynski, "Diffusional kurtosis imaging: the quantification of non-gaussian water diffusion by means of magnetic resonance imaging," Magn Reson Med **53**, 1432–40 (2005).

[23] Sune Nørhøj Jespersen, Henrik Lundell, Casper Kaae Sønderby, and Tim B Dyrby, "Orientationally invariant metrics of apparent compartment eccentricity from double pulsed field gradient diffusion experiments," NMR Biomed **26**, 1647–62 (2013).

[24] Samo Lasi**v**c, Filip Szczepankiewicz, Stefanie Eriksson, Markus Nilsson, and Daniel Topgaard, "Microanisotropy imaging: quantification of microscopic diffusion anisotropy and orientational order parameter by diffusion mri with magic-angle spinning of the q-vector," Frontiers in Physics **2**, 11 (2014).

[25] Enrico Kaden, Frithjof Kruggel, and Daniel C Alexander, "Quantitative mapping of the per-axon diffusion coefficients in brain white matter," Magnetic resonance in medicine (2015).

[26] Enrico Kaden, Nathaniel D. Kelm, Robert P. Carson, Mark D. Does, and Daniel C. Alexander, "Multi-compartment microscopic diffusion imaging," NeuroImage **139**, 346 – 359 (2016).

[27] A Bohr and Ben R Mottelson, *Nuclear Structure, Vol. II: Nuclear Deformations* (World Scientific, 1998).

[28] Nathan P. Skinner, Shekar N. Kurpad, Brian D. Schmit, L. Tugan Muftuler, and Matthew D. Budde, "Rapid in vivo detection of rat spinal cord injury with double-diffusion-encoded magnetic resonance spectroscopy," Magnetic Resonance in Medicine **DOI:10.1002/mrm.26243**, n/a–n/a (2016).

[29] Bibek Dhital, Elias Kellner, Marco Reisert, and Valerij G Kiselev, "Isotropic diffusion weighting provides insight on diffusion compartments in human brain white matter in vivo," Proceedings of the International Society of Magnetic Resonance in Medicine 23, p. 2788. (2015).

[30] Filip Szczepankiewicz, Samo Lasi**v**c, Danielle van Westen, Pia C Sundgren, Elisabet Englund, Carl-Fredrik Westin, Freddy St**r**ahlberg, Jimmy Lätt, Daniel Topgaard, and Markus Nilsson, "Quantification of microscopic diffusion anisotropy disentangles effects of orientation dispersion from microstructure: applications in healthy volunteers and in brain tumors," NeuroImage **104**, 241–252 (2015).

[31] Filip Szczepankiewicz, Danielle van Westen, Elisabet Englund,

Carl-Fredrik Westin, Freddy Strahlberg, Jimmy Lätt, Pia C. Sundgren, and Markus Nilsson, "The link between diffusion {MRI} and tumor heterogeneity: Mapping cell eccentricity and density by diffusional variance decomposition (divide)," NeuroImage , – (2016).

[32] Marco Reisert, Valerij G Kiselev, Bibek Dihtal, Elias Kellner, and DS Novikov, "Mesoft: unifying diffusion modelling and fiber tracking," in *Medical Image Computing and Computer-Assisted Intervention–MICCAI 2014* (Springer, 2014) pp. 201–208.

[33] Dmitri B Chklovskii, Thomas Schikorski, and Charles F Stevens, "Wiring optimization in cortical circuits," Neuron **34**, 341–7 (2002).

[34] Itamar Ronen, Matthew Budde, Ece Ercan, Jacopo Annese, Aranee Techawiboonwong, and Andrew Webb, "Microstructural organization of axons in the human corpus callosum quantified by diffusion-weighted magnetic resonance spectroscopy of n-acetylaspartate and post-mortem histology," Brain Struct Funct **219**, 1773–85 (2014).

[35] Marco Reisert, Elias Kellner, Bibek Dhital, Jürgen Hennig, and Valerij G. Kiselev, "Diffusion MRI: Disentangling micro- from mesostructure and bayesian parameter evaluation," Proceedings of the International Society of Magnetic Resonance in Medicine 24, p. 1999. (2016).

[36] Kip S Thorne, "Multipole expansions of gravitational radiation," Reviews of Modern Physics **52**, 299–339 (1980).

[37] Jelle Veraart, Jeny Rajan, Ronald R Peeters, Alexander Leemans, Stefan Sunaert, and Jan Sijbers, "Comprehensive framework for accurate diffusion mri parameter estimation," Magn Reson Med **70**, 972–84 (2013).

[38] Valerij G Kiselev, "Diffusion MRI: Theory, methods and applications," (Ed. Jones, D. K., Oxford University Press, New York, 2010) Chap. 10. The cumulant expansion: An overarching mathematical framework for understanding diffusion NMR.

[39] Jelle Veraart, Els Fieremans, and Dmitry S Novikov, "Diffusion MRI noise mapping using random matrix theory," Magnetic resonance in medicine **DOI: 10.1002/mrm.26059** (2016).

[40] Cheng Guan Koay and Peter J Basser, "Analytically exact correction scheme for signal extraction from noisy magnitude MR signals," Journal of Magnetic Resonance **179**, 317–322 (2006).

[41] Elias Kellner, Bibek Dhital, Valerij G Kiselev, and Marco Reisert, "Gibbs-ringing artifact removal based on local subvoxel-shifts," Magnetic resonance in medicine **DOI:10.1002/mrm.26054** (2015).

[42] Jelle Veraart, Els Fieremans, Ileana O Jelescu, Florian Knoll, and Dmitry S Novikov, "Gibbs ringing in diffusion MRI," Magnetic resonance in medicine **DOI: 10.1002/mrm.25866** (2015).

[43] Stephen M Smith, Mark Jenkinson, Mark W Woolrich, Christian F Beckmann, Timothy EJ Behrens, Heidi Johansen-Berg, Peter R Bannister, Marilena De Luca, Ivana Drobnjak, David E Flitney, *et al.*, "Advances in functional and structural MR image analysis and implementation as FSL," Neuroimage **23**, S208–S219 (2004).

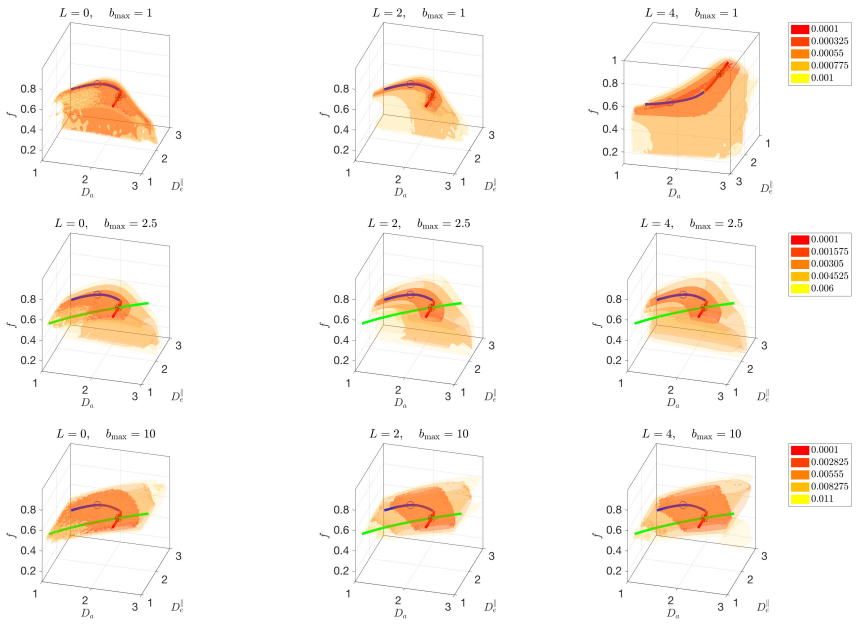


FIG. S1. **Low-energy landscape of the problem (6).** The F-values are minimized with respect to $D_e^{\perp}$ and p_l, for the case when the two branches form a single trench within the feasible parameter range. Ground truth values $\{f, D_a, D_e^{\parallel}, D_e^{\perp}, p_2\} = \{0.7, 2.4, 1.5, 0.8, 0.7\}$ correspond to three identical fiber segments crossing at an angle $\theta \approx 27^\circ$ to the tract axis. The simulated b-values correspond to those in our human experiments (see *Methods*), with all the 21 b-shells uniformly rescaled to attain the maximal value $b_{\max}$, such that the bottom row corresponds to the actual acquisition. The two analytical LEMONADE branches (+ red, - blue) match the low-value manifolds, especially for low $b_{\max}$. Increasing L, the 2-dimensional surface ($L = 0$, corresponding to the two constraints (18a) and (18c) for 4 scalar parameters) gradually turns into 1-dimensional trenches (the full system (18)), while increasing $b_{\max}$ causes flattening of the landscape such that it eventually follows the surface $f/\sqrt{D_a} = \text{const}$ dominated by the intra-axonal water[21], with the extra-axonal water exponentially suppressed (green line).

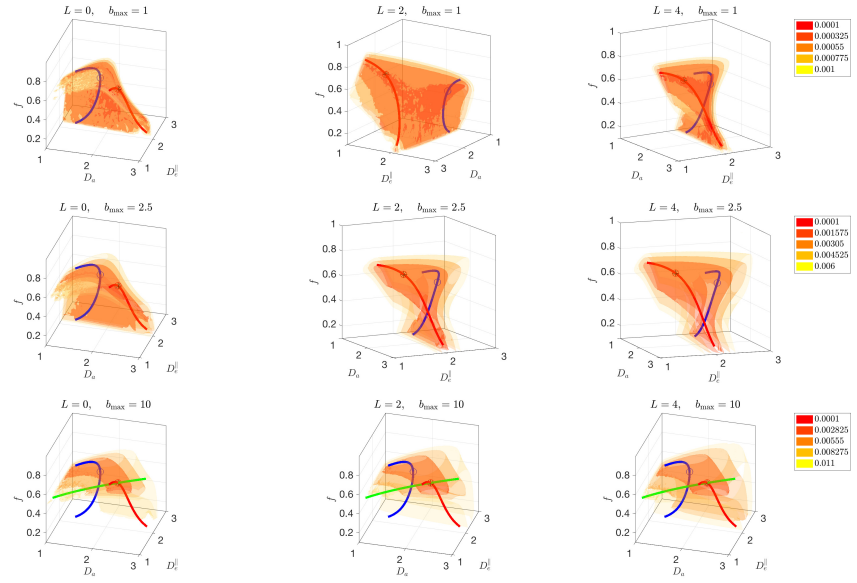


FIG. S2. The same as in Fig. S1 but with $D_e^{\perp} = 0.4$. The landscape is highly sensitive to the ground truth values: merely altering one parameter, $D_e^{\perp}$, we now have two separate trenches passing through the physically feasible parameter range. They eventually connect (as in Fig. S1), albeit outside this range. In this case it is particularly easy for spurious minima (e.g. due to noise) to appear in-between the trenches.

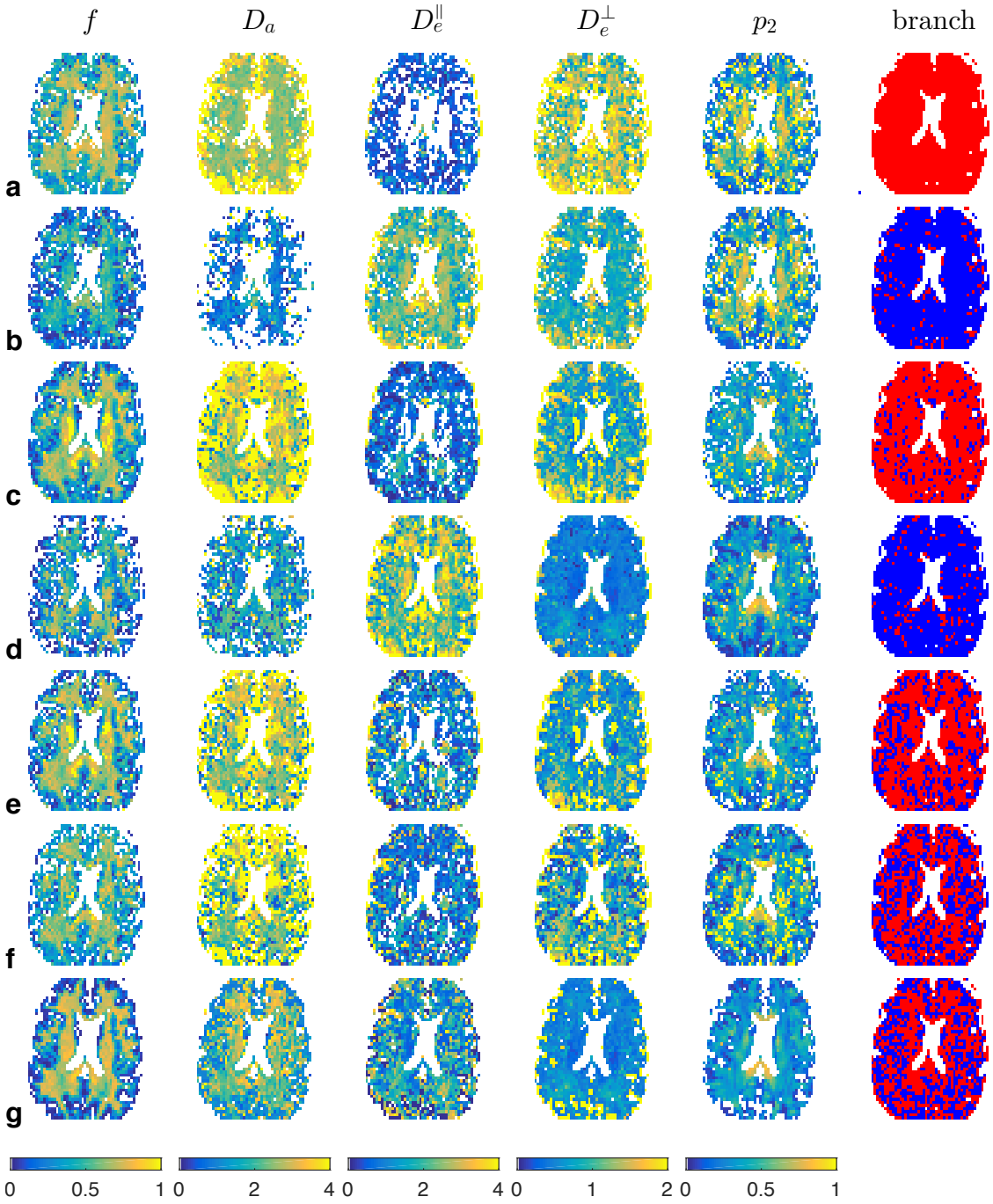


FIG. S3. **Processing steps: Maps for both branches and prevalence maps.** Exemplary maps for subject 1, mid-brain axial slice. **a,b:** outputs of LEMONADE $\zeta = \pm$ branches, respectively, equations (18), using only the shells within $0 \leq b \leq 2.5$ (see *Methods*). Note that $f_+ > f_-$, as well as $D_{a+} > D_{e+}^{\parallel}$ and $D_{a-} < D_{e-}^{\parallel}$, practically consistent with equation (7). For $\zeta = +$ branch, the output $D_e^{\parallel} < D_e^{\perp}$ is likely to be a result of the bias of moments estimation (a similar bias was observed in numerical simulations), since it is biophysically more plausible that $D_e^{\parallel} \gtrsim D_e^{\perp}$. **c,d:** RotInv $\zeta = \pm$ outputs of gradient-descent nonlinear minimization, equation (6), using all b shells, initialized via the corresponding LEMONADE maps. We observe the same qualitative features as in the LEMONADE maps, except for increasing $D_e^{\parallel}$ and decreasing $D_e^{\perp}$ for the $\zeta = +$ branch. Importantly, the branch index ζ ("branch" column), calculated using equation (7) is stable (cf. histograms in Fig. 3) — for the vast majority of voxels, the nonlinear fitting of the full problem (6) does not change the LEMONADE-assigned branch index $\zeta = \pm$ (red/blue). **e:** Combining the RotInv maps for $\zeta = \pm$ for WM/GM, respectively, see text. **f:** The same combination of the $\zeta = \pm$ RotInv maps for WM/GM, but now calculated only based on the $0 \leq b \leq 2.5$ measurements, a proxy for a clinically feasible acquisition. While the results are noisier, the overall correspondence with the full acquisition is evident. **g:** Prevalence maps. Rows **f** and **g** are the same as in Fig. 4, shown here for completeness.

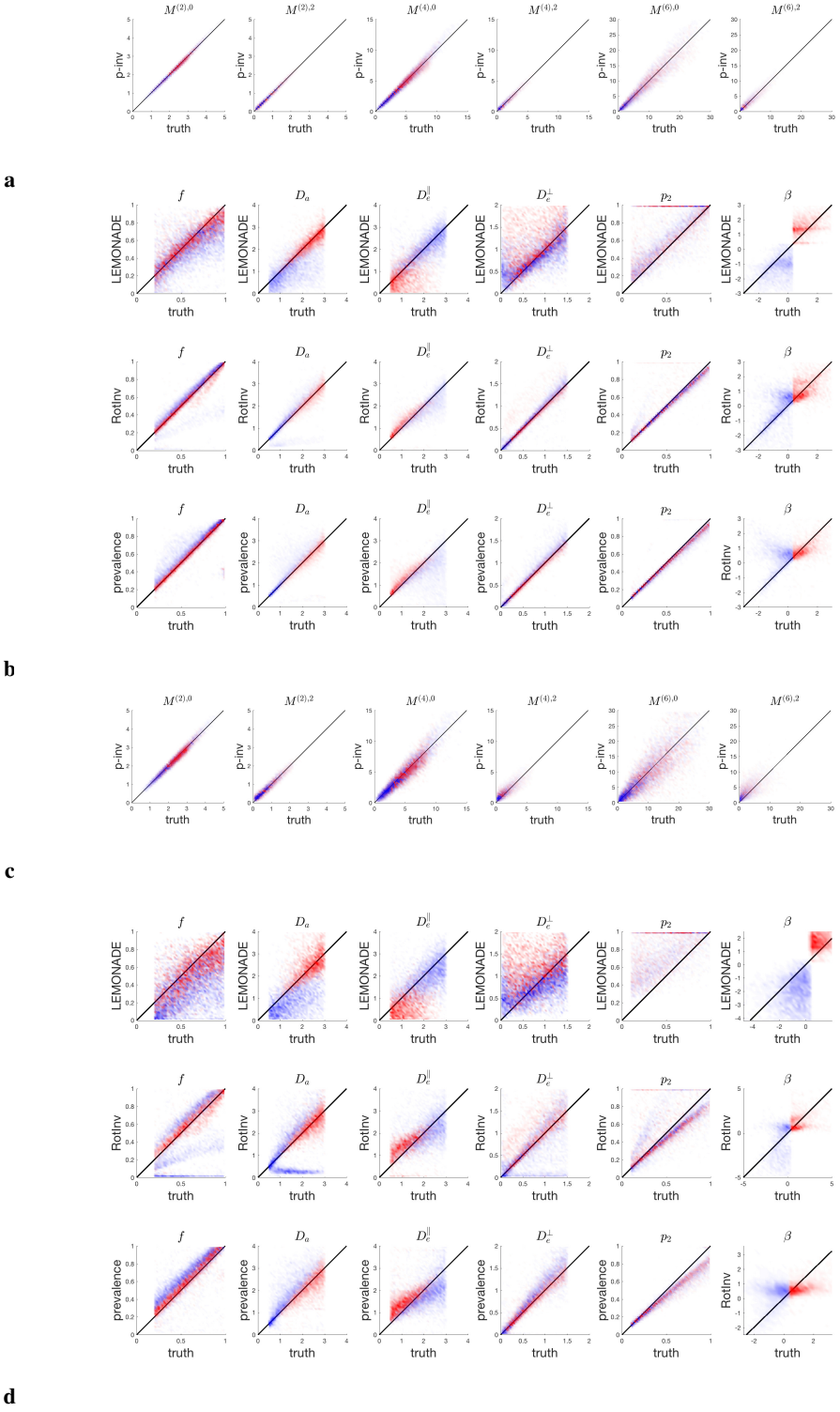


FIG. S4. **Noise propagation** for **a, b**: SNR = 100; **c, d:** SNR = 33, in estimating moments (panels **a** and **c**) and biophysical parameters (**b** and **d**). Results are from Monte Carlo simulations of the full MRI protocol (see *Methods*) with 10,000 random combinations of ground truth values uniformly distributed within the biophysically relevant intervals (x-axis, "truth"). The fiber geometry is three identical fiber segments with azimuthal angles $\phi = 0, \pm 2\pi/3$, crossing at an angle $\theta \approx 27^\circ$ with respect to the tract axis, as in Figs. S1 and S2. Gaussian noise with variance σ^2 is addded to both real and imaginary parts of the signal, with absolute value at $b = 0$ normalized to SNR $= 1/\sigma$, such that the magnitude signal follows Rician distribution. Red/blue colors correspond to $\zeta = \pm$ branches assigned based on the ground truth values according to equation (7). *Branch degeneracy manifests itself in that branch assignment is not apparent at the level of the rotational invariants – i.e. the moments (***a** *and* **c***) – and becomes evident based on the parameter values (***b** *and* **d***)*: practically, $\zeta = +$ corresponds to $D_a > D_e^{\parallel}$ and vice-versa, cf. equation (7). In panels **b** and **d**, top row corresponds to parameter estimation based on LEMONADE output, which subsequently served as initialization for the nonlinear fitting of equation (6) (middle row), where the LEMONADE branch was pre-selected based on the ground truth values. We can see that noise results in decrease of precision, and that it can accidentally switch the branch. Addition of nonlinear fit (6) notably improves both accuracy and precision relative to LEMONADE. Bottom row corresponds to the prevalence method, by starting at 20 random initializations within the physically relevant domain of parameters. Generally, intra-axonal parameters f and D_a are more precise than extra-axonal $D_e^{\parallel}$ and $D_e^{\perp}$; unfortunately, the branch ratio β is particularly imprecise, prompting the need for "orthogonal" measurements.